Catalysis Communications xxx (xxxx) xxx

Contents lists available at ScienceDirect

Catalysis Communications

journal homepage: www.elsevier.com/locate/catcom

Effects of alloying palladium with gold in furfural hydrogenation:An in situ ATR-IR spectroscopy and density functional theory study

Sebastiano Campisi [a,1], Silvio Bellomi [a,1], Lidia E. Chinchilla [b], Marta Stucchi [a], Laura Prati [a], Alberto Roldan [c], Davide Ferri [d], Alberto Villa [a,*]

[a] Dipartimento di Chimica, Università degli Studi di Milano, I-20133 Milano, Italy
[b] Departamento de Ciencia de los Materiales, Ingeniería Metalúrgica y Química Inorgánica, Facultad de Ciencias, Universidad de Cádiz, Campus Río San Pedro, Puerto Real (Cádiz), E-11510, Spain
[c] Cardiff Catalysis Institute, School of Chemistry, Cardiff University, CF10 3AT Cardiff, UK
[d] Paul Scherrer Institut, CH-5232 Villigen PSI, Switzerland

ARTICLE INFO

Keywords:
Adsorption
Biomass
Heterogeneous catalysis
Nano-alloys
Site isolation
Structure-activity
Surfaces

ABSTRACT

Furfural is a versatile platform molecule and a model compound to explore the key factors influencing activity and selectivity in heterogeneous catalysis. In this study, Pd and AuPd nanoparticles (average size 3.5–4 nm) were deposited on TiO_2 by sol immobilization method and were evaluated for liquid-phase furfural hydrogenation. Alloying Au and Pd caused a decrease in activity, an enhancement in stability, and a change in selectivity, favouring the complete hydrogenation of furfural over the decarbonylation reaction. These variations in catalytic performance were elucidated by combining in situ attenuated total reflectance infrared spectroscopy and density functional theory studies.

1. Introduction

There has been a notable surge in scientific exploration within biomass valorization in recent decades [1,2]. Substantial strides have been achieved in pinpointing "platform molecules," the fundamental building blocks derived from sugars through chemo-catalytic conversion [3–5]. As the significance of biomass-based industrial chemistry continues to grow, attention is increasingly focused on process optimization and overcoming associated challenges [6–8]. Dedicated efforts have been directed towards researching and refining reactive processes to enhance the functional versatility of these platform molecules. Chemicals derived from biomass have demonstrated utility across diverse applications, spanning pharmaceuticals, solvents, fuels, and fine chemicals.

A noteworthy example of a platform molecule is furfural (FF, furan-2-carbaldehyde), which is emblematic of the multifaceted landscape of biomass-derived compounds and their potential industrial applications [9–16]. The multifunctionality inherent in the furfural molecule presents an outstanding opportunity for many chemical transformations, yielding a diverse array of high-value products. However, at the same time, its high reactivity poses a classic challenge in heterogeneous catalysis, highlighting the difficulty in achieving selectivity. An integral aspect of this pursuit is the design of efficient and selective catalysts, representing a significant goal in current research projects [17–20]. Furfural molecules can adsorb on catalytic surfaces through their functional groups, carbonyl group and furanic ring, forming a variety of products (Fig. S.1) [21]. Specifically, when subjected to hydrogenation conditions on noble metal catalysts, the aromatic furan ring tends to adhere to the metallic surface firmly. Therefore, FF hydrogenation results in the dominant production of furan (F) and tetrahydrofuran (THF) through processes such as decarbonylation and ring hydrogenation. Depending on the catalyst composition and structure, reactions such as aldehyde hydrogenation and hydrodeoxygenation drive the conversion of furfuryl oxygenates to desirable fuels, furfuryl alcohol (FA) or methylfuran (MF) [22–27].

Various strategies have been employed to control selectivity in furfural hydrogenation over noble metal-based catalysts: From utilizing bimetallic catalysts [28] and fine-tuning size and shape [29] to leveraging support cooperative action [30,31] and incorporating surface modifiers [32–34]. Specifically, the synergistic interplay between Pd

* Corresponding author.
E-mail address: alberto.villa@unimi.it (A. Villa).
[1] These authours equally contributed to the work.

https://doi.org/10.1016/j.catcom.2024.106894
Received 29 December 2023; Received in revised form 28 February 2024; Accepted 2 March 2024
Available online 4 March 2024

and a second metal (e.g., Ni, Cu, Ag) has showcased tremendous potential in steering selectivity towards particular products in furfural hydrogenation [35–48].

In this study, gold (Au) was incorporated into the inherently active palladium (Pd) catalysts to generate AuPd nanoparticles (NPs) of similar size, which were then supported on titanium dioxide (TiO_2). The alloying of palladium with gold has proven effective in altering the activity and selectivity of catalysts, thereby enhancing their stability in various liquid-phase oxidation and hydrogenation reactions [49–55]. Recent findings indicated a predominant product, 2-methyloxolan-2-ol, from the catalytic hydrogenation of furfural using bimetallic AuPd NPs supported on silica [56]. Additionally, the introduction of titanium (Ti) into AuPd/SiO_2 promoted a ring-opening pathway, leading to the formation of 1,2-pentanediol [57]. Herein, we revealed the modification effects of AuPd NPs on TiO_2 support through in situ Attenuated Total Reflectance (ATR) FT-IR spectroscopy and Density Functional Theory (DFT) atomistic simulations. These techniques enabled the correlation of adsorption energies with surface species evolution, the catalytic activity, and the selectivity observed in batch tests.

2. Experimental method

2.1. Catalyst preparation

2.1.1. Monometallic catalysts

2.1.1.1. Au catalyst preparation. Solid $NaAuCl_4$ * $2H_2O$ (Aldrich, 99.99% purity; 0.043 mmol) and polyvinyl alcohol solution (PVA, MWPVA = 13,000-23,000, 87–89% hydrolyzed, Aldrich; 1% *w*/w; Au/PVA 1:0.5, *w*/w) were combined in 100 mL H_2O. After 3 min, a solution of sodium borohydride $NaBH_4$ (Fluka, > 96%; Au/$NaBH_4$ 1/4 mol/mol) was introduced with vigorous magnetic stirring, resulting in the immediate formation of a ruby red Au(0) sol. A UV–visible spectrum confirmed the complete reduction of $AuCl_4^-$ and the emergence of the plasmon peak of Au(0) nanoparticles. The colloids, acidified to pH 2 with sulfuric acid, were rapidly immobilized by adding the support (TiO_2, Degussa P25, 49 $m^2\ g^{-1}$, 80% anatase) under vigorous stirring. The support amount was calculated to achieve a final metal loading of 1 wt%. Catalysts were filtered, washed, and dried at 80 °C for 4 h.

2.1.1.2. Pd catalyst preparation. Solid Na_2PdCl_4 (Aldrich, 99.99% purity; Pd 0.043 mol) and PVA solution (1% *w*/w) (Pd/PVA 1:0.5 w/w) were mixed in 100 mL H_2O. After 3 min, NaBH4 (Pd/NaBH4 = 1/8 mol/mol) was added to the yellow-brown solution with vigorous magnetic stirring, immediately forming a brown Pd(0) sol. A UV–visible spectrum confirmed complete $PdCl_4^{2-}$ reduction. The colloids, acidified to pH 2 with sulfuric acid, were rapidly immobilized by adding the carrier with vigorous stirring. The carrier amount was calculated to achieve a final metal loading of 1 wt%. Catalysts were filtered, washed, and dried at 80 °C for 4 h.

2.1.2. Bimetallic catalysts

Bimetallic catalysts were prepared following a previously reported procedure. After the preparation of 0.73 wt% Au/TiO_2, the material was dispersed in 100 mL water, and Na_2PdCl_4 (Pd 0.025 mol) and PVA solutions (1%, *w*/w) (Pd/PVA 1:0.5 w/w) were added. Hydrogen (H_2) was bubbled under atmospheric pressure and room temperature (50 mL min^{-1}). After 2 h, the slurry was filtered, and the catalyst was thoroughly washed with distilled water. Inductively coupled plasma (ICP) analyses were performed on the filtrate to verify the quantitative metal loading on the support. The final total metal loading was 1 wt% in all cases, with an Au/Pd mass ratio of 7.3/2.7 (6/4 mol/mol) for the bimetallic catalyst. The metal content was assessed by by ICP-OES using a Perkin Elmer Optima 5300 DV instrument.

2.2. Catalytic test in batch reactor

The hydrogenation of furfural was carried out at 50 °C in a stainless-steel reactor (30 mL capacity) equipped with a heater, a mechanical stirrer, a gas feed system and a thermometer. A fresh solution of furfural (10 mL, 0.3 M in 2-propanol) was added to the reactor with the desired amount of catalyst (furfural/metal = 500 mol/mol). The reaction vessel was rinsed three times with 3 bar N_2 before it was depressurised and again pressurised with 1 bar H_2 and sealed. The mixture was thermostated at 50 °C before being mechanically stirred (1000 rpm) to ensure kinetic regime conditions. At the end of the reaction, the autoclave was cooled to room temperature (25 °C) and the pressure was released. The process of pressurising the vessel was repeated after taking each reaction sample. The reaction samples (0.2 mL) were taken at regular intervals and mixed with the internal solvent (2-propanol) and the external standard (dodecanol) before being analysed in an Agilent 6890 gas chromatograph (Agilent Technologies, Santa Clara, California, United States) using a Zebron ZBS 60 m × 0.32 mm × 1 μm column (Phenomenex, Torrance, California, United States). Authentic products (e.g., FA and THFA) were analysed to determine retention times. Quantitative analyses were performed using the external standard method, comparing the GC peak area of each product with that of a known standard (dodecanol). Unidentified ether products were identified by gas chromatograph-mass spectroscopy (GC–MS). Aliquots of the reaction mixture were analysed using a Thermo Scientific ISQ QD (Thermo Fisher Scientific, Waltham, Massachusetts, United States), equipped with an Agilent VF-5 ms column, 60 m × 0.32 mm × 1 μm (inner diameter thickness) (Agilent Technologies, Santa Clara, California, United States).

2.3. Catalyst characterization

A home-built batch reactor cell was used to monitor the progress of furfural hydrogenation both at the catalyst surface and in solution using attenuated total reflectance (ATR-IR) [53]. The cell modifies the one described in Ref. [58]. In this case, stirring was obtained with a conventional laboratory magnetic stirrer integrated into the bottom plate of the cell. The top of the cell was then fitted with a cylindrical stainless-steel body and a stainless steel lid, allowing the insertion of a glass condenser (conical cone ground, 19/26) for experiments under reflux. The ZnSe internal reflection element (IRE, 30°, 50 mm × 20 mm × 2 mm; Crystran Ltd., Poole, United Kingdom) was coated with a powder film obtained by evaporating a catalyst suspension (10 mg/ 2 mL suspension) and placed on the horizontal heatable bottom of the cell (Fig. S.2). After placing the cell body and adding 10 mL of 2-propanol as the solvent, the temperature was raised to 50 °C, and the system was kept under H_2 bubbling for about 30 min with reflux and stirring. Before injection of furfural (20 mM), a background spectrum of the catalyst was recorded at 50 °C in 2-propanol. Then, a series of consecutive ATR-IR spectra (200 scans, about 4 min/spectrum, 4 cm^{-1} resolution) were recorded to follow the reaction. At about 5 min after the injection of furfural, N_2 was replaced by 1 bar H_2, and the system was allowed to react for about two h.

CO adsorption at 50 °C was followed by flowing 2-propanol saturated with 5 vol% CO/Ar bubbling at 1 bar through a home-made flow-through ATR-IR cell equipped with a ZnSe IRE (45°, 52 mm × 20 mm × 2 mm). Prior to CO adsorption [53], the catalyst layer deposited onto the IRE was reduced with a 2-propanol solution saturated with H_2 bubbling at 1 bar at 75 °C for 1 h.

Samples for transmission electron microscopy (TEM) studies were prepared by depositing small amounts of dry catalyst powder onto holey carbon copper grids. Micrographs combined with analytical studies by energy-dispersive X-ray (XEDS) and electron energy loss spectroscopy were performed in High Annular Dark Field mode using a FEI Titan^3 80–300 microscope operated at 200 and 80 kV. Digital Micrograph, TIA, and INCA software were used to analyse the TEM micrographs and XEDS

Table 1
Catalytic results in furfural hydrogenation.

Catalyst[a]	Particle size[b] (nm)	Conversion[c] (%)	Selectivity (%)[d]					
			FA	THFA	2-MF	2-MTHF	FIE	furan
1 wt% Au/TiO_2	3.7 ± 0.9	2	–	–	–	–	>99	
1 wt% Pd/TiO_2	3.5 ± 0.7	80	76.2	2.3	7.1	0.4	4.8	5.2
1 wt% Au_6Pd_4/TiO_2	4.1 ± 1.2	55	68.2	22.1	1.2	3.1	4.2	0.2

[a] Reaction conditions: Furfural = 0.3 M; FF/metal ratio = 500 wt/wt, 50 °C, 1 bar H_2.
[b] Data from Ref. [53].
[c] Conversion after 3 h.
[d] Selectivity at 80% of conversion.

spectra. The quantification of XEDS spectras was processed by using the theroretical Cliff-Lorimer factors using the Au-M and Pd-L family lines. The PSD, Gaussian fit, average particle diameter, and metal dispersion were calculated using Gauss software, assuming a truncated cuboctahedron particle shape. EELS data were acquired in Dual mode in order to have two core –loss regions for collection of the characteristic signals of Ti-$L_{3,2}$ at 45 eV and Pd-$M_{5,4}$ at 335 eV, simultaneously at high energy to obtained the typical signals of Au-$M_{4,5}$ at 2206 Ev. Post treatment of these data, such as background subtraction, multiple linear least square (MLLS) fitting along principal component analysis (PCA), were processed using Gatan's Digital Micrograph.

2.4. Computational method

All the periodic density functional theory (DFT) calculations were carried out using VASP (Vienna Ab initio Software Package) [59–61]. The Perdew–Burke–Ernzerhof (PBE) exchange-correlation functional [62] was employed to account for the exchange and correlation effects on valence electrons with the projector augmented-wave method used to represent atomic core states [63,64]. Dispersion effects were included using Grimme's empirical DFT-D3 model [65]. FCC lattice constants were estimated to be 3.88 Å (experimental value of 3.89 Å) and 3.99 Å for Pd and AuPd, respectively. All lattice constants were estimated by fitting single-point calculations at fixed lattice constants to the Murnaghan equation of state. All lattice constant calculations employed the tetrahedron method with Blöchl corrections and a gamma-centred 15x15x15 k-point mesh. Binding energies and activation energies were calculated with close-packed (111) slabs of Pd and mixed AuPd (with an Au:Pd ratio of 1:1) in 4 × 4 supercells (sixteen atoms in each layer) and a total of four atomic layers, with the bottom two layers fixed in their bulk positions and the top two layers and adsorbates (if present) allowed to relax. Slabs were separated vertically by 15 Å of vacuum [66]. For slab calculations, a gamma-centred Monkhorst-Pack scheme with a 4x4x1 k-point mesh was used. All slab calculations employed Gaussian smearing with a smearing parameter of 0.05 eV. The periodically repeated slabs were separated by a 20 Å vacuum layer along the Z direction, which is enough to avoid any spurious interaction with periodically replicated images. A kinetic energy of the plane waves was set to 400 eV ensuring no Pulay stress. The convergence criterion was set such that the calculations converge when the forces are <0.02 eV $Å^{-1}$ for adsorption calculations, 0.001 eV $Å^{-1}$ for the bulk, and 0.01 eV $Å^{-1}$ for surface optimization calculations. The adsorption energy was computed using Eq. (1).

$$E_{ads} = E_{sys} - (E_s + E_{molec}) \quad (1)$$

Where E_{sys} is the energy of the adsorbate adsorbed on the slab, E_s is the energy of the bare slab and E_{molec} is the energy of the adsorbate in the gas phase, that is, in a cell large enough to avoid intermolecular interactions.

3. Results and discussion

3.1. Monometallic and bimetallic catalysts and their performance in the hydrogenation of furfural

A 1 wt% $AuPd/TiO_2$ catalyst (Au:Pd molar ratio 6:4, verified by ICP analysis) was synthesized through a two-step procedure [52]. This bimetallic catalyst was compared to monometallic counterparts (Au and Pd catalysts) with an equivalent total metal content of 1%.

Monometallic and bimetallic catalysts exhibited comparable mean particle sizes ranging from 3.5 to 4.1 nm [53]. This is a typical feature of catalysts synthesized using the specific sol-immobilization procedure employed in this study [52].

The elemental distribution of chemical constituents in the bimetallic NPs was analysed using Electron Energy Loss Spectroscopy (EELS) and XEDS analysis. For example, the spatial distribution of Au and Pd resulting from Pd-$M_{4,5}$ and Au-$M_{5,4}$ EELS signals is illustrated in colored maps in Fig. S.4a. In this example, the EELS mapping revealed a homogeneous distribution of Pd and Au throughout the entire particle, with no discernible segregation, confirming the presence of AuPd alloys. Further details of the bimetallic entities are discussed in light of additional data.

The catalytic performance towards the liquid-phase hydrogenation of furfural was assessed in a batch reactor utilizing 2-propanol as the solvent ($T = 50$ °C, 1 bar H_2). Under these reaction conditions, Au/TiO_2 demonstrated low activity, achieving only a 2% conversion after 3 h (Table 1). In contrast, Pd/TiO_2 achieved 80% conversion after the same time. The combination of Au and Pd (Au/Pd molar ration 6:4) resulted in a moderately active catalyst, ensuring a furfural conversion of 55%, positioned between its monometallic counterparts of Au and Pd.

Regarding selectivity, the etherification reaction, with the formation of isopropryl-ether (FIE) dominated the monometallic Au catalyst, a characteristic often observed in furfural hydrogenation at low conversion values [67]. Furfuryl alcohol (FA) emerged as the predominant product with Pd and AuPd catalysts, displaying selectivity values, calculated at 80% of conversion, ranging from 68% to 76%. However, a notable divergence in by-product distribution is evident from the selectivity data in Table 1. Monometallic Pd exhibited the production of deoxygenated products, 2-methylfuran (7% selectivity) and furan (5% selectivity). In contrast, the AuPd system facilitated the hydrogenation of the furan ring, resulting in a selectivity increase towards tetrahydrofurfuryl alcohol (THFA; ca. 20% selectivity, Fig. S.5a) and 2-methyltetrahydrofuran (2-MTHF; ca. 3%), while the formation of 2-methylfuran and furan was negligible.

Stability tests were carried out through eight consecutive runs employing the bimetallic catalyst. The catalyst demonstrated consistent stability, exhibiting negligible signs of deactivation throughout the successive runs. Intriguingly, the selectivity towards FA and THFA remained unaltered even after the completion of all eight runs (Fig. S.5b). Contrarily to the Pd/TiO_2 rapid deactivates due to the generation of Pd carbide, fostering a less favourable furfural adsorption configuration (Fig. S.5c) [68]. The enhanced stability attributed to the inclusion of Au aligns with findings documented in prior literature.

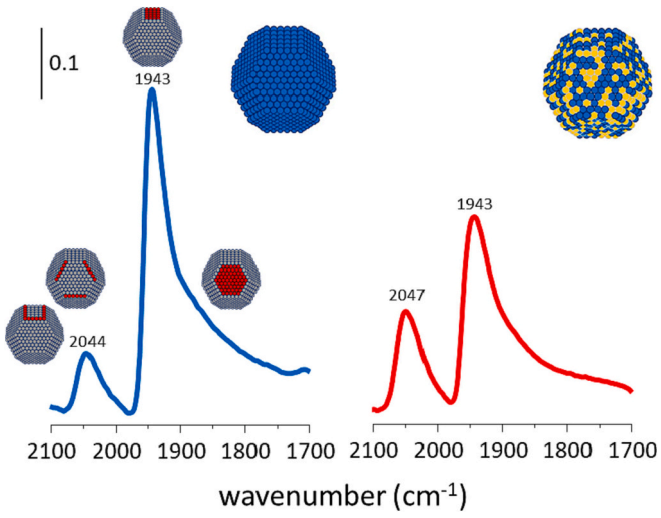

Fig. 1. ATR spectra of adsorbed CO on Pd/TiO_2(blue curve, left), $AuPd/TiO_2$ (red curve, right). (For interpretation of the references to colour in this figure legend, the reader is referred to the web version of this article.)

3.2. Structure of Pd and AuPd catalysts

In the pursuit of unravelling the structural factors influencing activity and selectivity, the influence of particle sizes can be discounted, given the comparable size distribution observed in both Pd and AuPd NPs (Table 1).

Detailed structural features of these catalysts, as obtained through TEM techniques, can be found in the supporting information, particulary in Fig. S3, which includes HAADF-STEM and HRTEM images illustrating the typical morphology, size and crystalline structure of several particles of $AuPd/TiO_2$ catalysts. Upon analysis of the HRTEM images, distances of approximately 0.23 nm have been observed, which could correspond to the {111} planes of the face-centered cubic (fcc) structure of gold-rich entities, either in pure form or as alloys. Complementary information provided in Fig. S4a-b confirms the presence of such particles, indicating the existence of both monometallic Au and AuPd alloys.

As depicted in Fig. S4b, the catalysts exhibit a uniform distribution of particles ranging in size from 1 to 5 nm. Further analysis of individual particles reveals that the vast majority contain both Au and Pd metals, spanning compositions between 64 and 82 at.% Au, with only a small fraction being composed of pure monometallic particles. The corresponding average gold content in the bimetallic particles is approximately 72%, consistent with estimates obtained via CP-AES.

The discernible variations in activity and selectivity between supported Pd and AuPd catalysts could potentially be attributed to distinct surfaces, site exposure or site isolation effects arising from alloying. In support of this hypothesis, spectroscopic techniques such as EELS and XEDS analysis analysis have revealed the presence of Au-rich domains with random compositions on the bimetallic entities.

Using CO adsorption, it is possible to probe the available surface sites and characterize the adsorption features of the catalysts. In previous studies, diffuse reflectance infrared Fourier transform (DRIFT) spectroscopy with gas-phase CO has been used to characterize the surface exposure on Pd/TiO_2 and $AuPd/TiO_2$ catalysts [53]. From these studies, CO adsorption on metallic Pd typically yielded distinct bands, including linearly bound CO (CO_L) at corners ($\tilde{\nu}$ = 2097 cm^{-1}) and edges ($\tilde{\nu} \approx$ 2080 cm^{-1}), bridging bonded CO (CO_B) to Pd(100) facets ($\tilde{\nu}$ = 1981 cm^{-1}) and to step/edges ($\tilde{\nu}$ = 1952 cm^{-1}) and coordinated to partially oxidized Pd^{2+} sites. The absence of Pd^{2+} species in $AuPd/TiO_2$ suggested that Pd was less prone to oxidation upon alloying with Au. Introducing gold prompted also structural changes. The elevated CO_L/CO_B ratio on $AuPd/TiO_2$ agrees well with the less intense CO adsorption bands obtained on $AuPd/TiO_2$ compared to Pd/TiO_2, which is attributed to the lower content of Pd in the bimetallic catalyst (Au/Pd = 6/4 mol_{Au}/mol_{Pd}) as well as to Pd species closely interacting with Au through alloying.

The CO adsorption from the liquid phase (CO-saturated 2-propanol) on the catalysts was monitored at 50 °C to unravel the influence of the polar solvent (2-propanol) on adsorption sites and their behaviour under reaction conditions. As shown in Fig. 1, both spectra exhibited prominent bands at 1943 cm^{-1} and 2044 cm^{-1} (2047 cm^{-1} for $AuPd/TiO_2$), attributed to CO_B on Pd(100) and CO_L, respectively. Furthermore, a shoulder of the CO_B signal indicated the presence of hollow bonded CO (CO_{3B}) on Pd(111). A markedly higher CO_L/CO_B ratio in $AuPd/TiO_2$ than in Pd/TiO_2 suggested the existence of small Pd domains, i.e., with decreased Pd—Pd sites. Therefore, our data confirm site isolation effects in the bimetallic AuPd particles, i.e., the deposition of Pd onto preformed Au nanoparticles likely led to the formation of smaller and less continuous Pd domains. In addition, the use of CO as a probe molecule at

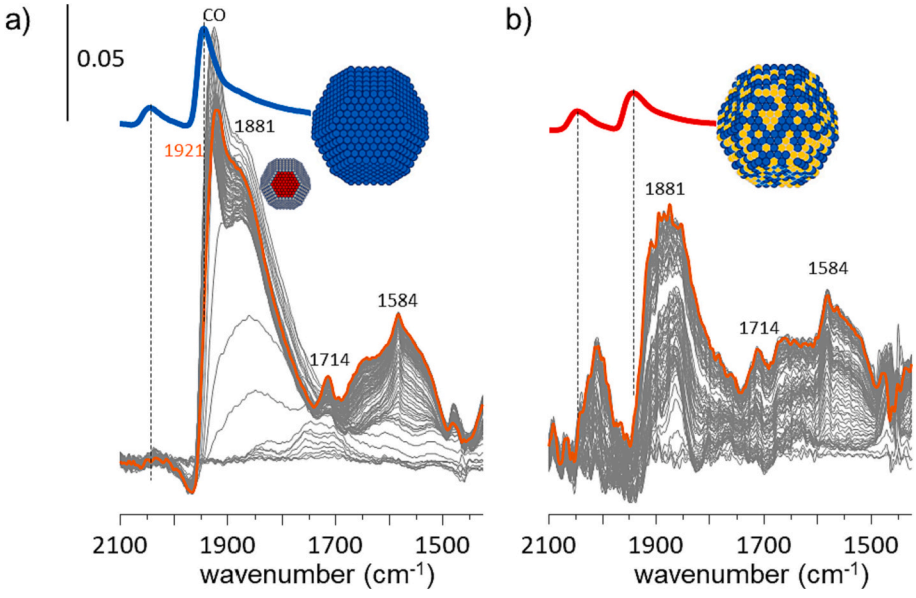

Fig. 2. In situ ATR-IR spectra during furfural hydrogenation on a) Pd/TiO_2 and b) $AuPd/TiO_2$.

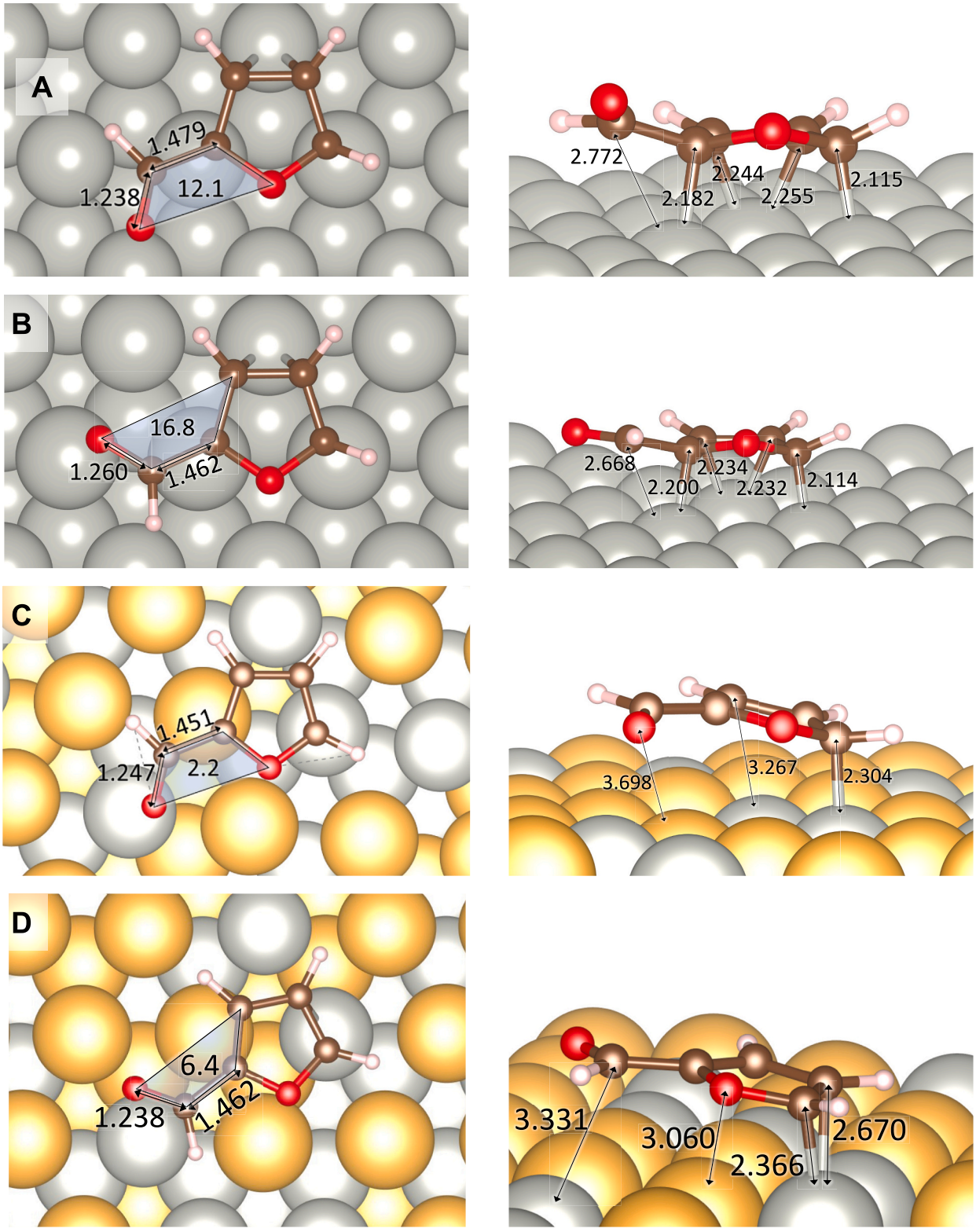

Fig. 3. Schematic representations of cis-furfural on (A) Pd(111) and (C) AuPd(111) and trans-furfural on (B) Pd(111) and (D) AuPd (111) model surfaces. Inset values indicate interatomic distances and angles in angstroms and degrees, respectively.

operating conditions allowed further investigation of the decarbonylation of furfural, which leads to the production of furan, observed as the main by-product.

3.3. *In situ* ATR-IR spectroscopy

The evolution of surface species during the hydrogenation of furfural was followed using ATR-IR spectroscopy on catalyst layers deposited on an internal reflection element on the bottom of a batch-reactor cell. In this setup, the catalyst layer was exposed to a 2-propanol solution of

Table 2
Most stable adsorption configurations (cis- and trans-) of adsorbed furfural on the different model slabs.

Surface	E_{ads} (eV)	
	cis	trans
Pd (111)	−2.42	−2.90
AuPd (111)	−1.90	−1.89

furfural (20 mM) at reflux conditions with a reaction time of 120 min, employing hydrogen bubbling instead of a pressurised suspension.

The in situ ATR-IR spectra (Fig. 2) obtained for the samples showed signals at 1714 cm^{-1} and 1584 cm^{-1}, characteristic of carbonyl stretching and furanic ring respectively, and ascribed to furfural dissolved in 2-propanol. The broad signal extending between 1700 and 1500 cm^{-1} is indicative of formation of adsorbed organic species whose nature and location (metal(s) vs support) need further analysis and experiments. The decarbonylation of furfural was studied through the intense signals of adsorbed CO in the 1800–2000 cm^{-1} region and compared to liquid and gas phase adsorption of molecular CO (Fig. 1) to unveil sites participation in the catalytic process. Specifically, in the case of Pd/TiO_2 catalyst, two intense signals at 1921 cm^{-1} and 1881 cm^{-1} can be ascribed to CO_B and CO_{3B}. The bathochromic shift by 20 cm^{-1} compared to CO adsorbed from the liquid phase (Fig. 1, top curves in Fig. 2) might be caused by changes in the electronegativity of the surface as a consequence of the presence of co-adsorbed hydrides and furfural in the reaction environment [69].

In contrast to CO adsorption from liquid phase, the intensity of CO_L signals (> 2000 cm^{-1}) was negligible during reaction. This lack of CO_L implies that the CO was generated and adsorbed selectively on specific sites, potentially the Pd(111) terraces. Therefore, these Pd(111) terraces can be identified as preferential sites for furfural decarbonylation on the Pd surface.

In the ATR-IR spectra collected over $AuPd/TiO_2$ signals at 1881 cm^{-1} and 2020 cm^{-1} can be associated with CO_B and CO_L, respectively. The CO_L/CO_B ratio was similar to that observed upon CO adsorption in the liquid phase (Fig. 1). The absence of the signal at 1921 cm^{-1} indicates that these sites can perform total furfural hydrogenation to THFA.

3.4. Atomistic simulations on Pd(111) and AuPd(111) surfaces

DFT calculations were performed to explore the interaction of furfural with monometallic and bimetallic surfaces and to rationalize the changes observed in activity and product selectivity. The Pd/TiO_2 catalyst was modelled with a Pd(111) metal slab. The $AuPd/TiO_2$ was modelled by a random AuPd alloy, i.e. the most stable configuration of several 50:50 arrangements tested, exposing the (111) surface [55].

The furfural initial adsorption configuration was set as η^2 - (C,O) aligned with previous benchmarks on (111) metal slabs and at low substrate and H_2 coverages [70,71]. On Pd(111), we observed adsorbed furfural to interact through the furanic ring (Fig. 3) preferentially; Table 2 contains the adsorption energies for both configurations, i.e. cis and trans, which are in entire agreement with previous reports [70]. Furfural adsorption on Pd leads to the activation of C_1 in the ring, as observed from the lost planarity and the slight elongation of the C—C distance compared to the gas phase furfural (1.456 Å). The distortion on the molecule and the marked exothermicity confirm the high affinity observed from the experiments and explain the preferential decarbonylation via the planar interaction of furfural through the entire furanic ring. When Au is incorporated and alloyed with Pd, the preferential sites are embedded in islands on the surface, as observed from in situ ATR-IR spectroscopy (Fig. 2), weakening the furfural binding energy independently of the molecular configuration, i.e. cis or trans. The adsorption energy and negligible distortion on the carbonyl side of the molecule align with the limited reactivity observed in the experiments and favoured ring hydrogenation on $AuPd/TiO_2$ [70]. Besides, and contrarily to the Pd surface, the plane of the molecule is not parallel to AuPd alloy as it mainly bonds with the portion of the furanic ring carbon atoms furthest from the carbonyl group.

4. Conclusions

Using in situ vibrational spectroscopy in liquid phase and computational methods, we have comparatively studied monometallic Pd/TiO_2 and bimetallic $AuPd/TiO_2$ catalysts for furfural hydrogenation. The Pd islands exposed on the surface upon alloying Au and Pd increased particle stability and suppressed C—C bond cleavage and decarbonylation reactions while simultaneously enhancing the total hydrogenation reaction. Both ATR-IR and DFT studies revealed that the difference in product distribution between the two catalysts could be ascribed to a different interaction strength between the aromatic ring of furfural and the metal surfaces as well as the availability of particular surface sites.

CRediT authorship contribution statement

Sebastiano Campisi: Writing – original draft, Investigation. **Silvio Bellomi:** Writing – original draft, Investigation, Formal analysis. **Lidia E. Chinchilla:** Formal analysis, Data curation. **Marta Stucchi:** Validation, Data curation. **Laura Prati:** Validation, Supervision. **Davide Ferri:** Writing – review & editing, Formal analysis, Conceptualization. **Alberto Villa:** Writing – review & editing, Conceptualization.

Declaration of competing interest

The authors declare that they have no known competing financial interests or personal relationships that could have appeared to influence the work reported in this paper.

Data availability

Data will be made available on request.

Acknowledgements

Authors are thankful to Lorenzo Landenna for the experimental work. The authors express their gratitude to G. Botton for invaluable support and to the facilities and technical staff of the Canadian Centre for Electron Microscopy (CCEM) at McMaster University. Supercomputing Wales is kindly acknowledged for access to the Hawk HPC facility, which is part-funded by the European Regional Development Fund via the Welsh Government. D.F. would like to thank PSI for financial support (CROSS project).

Appendix A. Supplementary data

Supplementary data to this article can be found online at https://doi.org/10.1016/j.catcom.2024.106894.

References

[1] R.A. Sheldon, Biocatalysis and biomass conversion: enabling a circular economy, Philos. Trans. R. Soc. A Math. Phys. Eng. Sci. 378 (2020) 20190274, https://doi.org/10.1098/rsta.2019.0274.
[2] B. Kumar, P. Verma, Biomass-based biorefineries: an important architype towards a circular economy, Fuel 288 (2021) 119622, https://doi.org/10.1016/j.fuel.2020.119622.
[3] S.H. Shinde, A. Hengne, C.V. Rode, Lignocellulose-derived platform molecules, in: S. Saravanamurugan, A. Pandey, H. Li, A.B.T.-B. Riisager, Biofuels, Biochemicals (Eds.), Biomass, Biofuels, Biochem, Elsevier, 2020, pp. 1–31, https://doi.org/10.1016/B978-0-444-64307-0.00001-9.
[4] Z. Zhou, D. Liu, X. Zhao, Conversion of lignocellulose to biofuels and chemicals via sugar platform: an updated review on chemistry and mechanisms of acid hydrolysis of lignocellulose, Renew. Sust. Energ. Rev. 146 (2021) 111169, https://doi.org/10.1016/j.rser.2021.111169.

[5] J.S. Luterbacher, D. Martin Alonso, J.A. Dumesic, Targeted chemical upgrading of lignocellulosic biomass to platform molecules, Green Chem. 16 (2014) 4816–4838, https://doi.org/10.1039/C4GC01160K.
[6] A. Al Ghatta, P.Y.S. Nakasu, J.P. Hallett, Implementation of furan-based building blocks in commodity chemical production: an opinion on scientific progress and economic viability, Curr. Opin. Green Sustain. Chem. 41 (2023) 100792, https://doi.org/10.1016/j.cogsc.2023.100792.
[7] R.G. Saratale, S.-K. Cho, R.N. Bharagava, A.K. Patel, S. Varjani, S.I. Mulla, D.S. Kim, S.K. Bhatia, L.F.R. Ferreira, H.S. Shin, G.D. Saratale, A critical review on biomass-based sustainable biorefineries using nanobiocatalysts: opportunities, challenges, and future perspectives, Bioresour. Technol. 363 (2022) 127926, https://doi.org/10.1016/j.biortech.2022.127926.
[8] R. Saini, C.S. Osorio-Gonzalez, K. Hegde, S.K. Brar, S. Magdouli, P. Vezina, A. Avalos-Ramirez, Lignocellulosic biomass-based biorefinery: an insight into commercialization and economic standout, Curr. Sustain. Energy Rep. 7 (2020) 122–136, https://doi.org/10.1007/s40518-020-00157-1.
[9] Z. Yang, J. Zhang, G. Qian, X. Duan, X. Zhou, Production of biomass-derived monomers through catalytic conversion of furfural and hydroxymethylfurfural, Green Chem. Eng. 2 (2021) 158–173, https://doi.org/10.1016/j.gce.2020.11.001.
[10] J. Long, W. Zhao, H. Li, S. Yang, Chapter 11 - Furfural as a renewable chemical platform for furfuryl alcohol production, in: S. Saravanamurugan, A. Pandey, H. Li, A.B.T.-B. Riisager, Biofuels, Biochemicals (Eds.), Biomass, Biofuels, Biochem, Elsevier, 2020, pp. 299–322, https://doi.org/10.1016/B978-0-444-64307-0.00011-1.
[11] M. Kabbour, R. Luque, Chapter 10 - Furfural as a platform chemical: From production to applications, in: S. Saravanamurugan, A. Pandey, H. Li, A.B.T.-B. Riisager, Biofuels, Biochemicals (Eds.), Biomass, Biofuels, Biochem, Elsevier, 2020, pp. 283–297, https://doi.org/10.1016/B978-0-444-64307-0.00010-X.
[12] X. Zhang, S. Xu, Q. Li, G. Zhou, H. Xia, Recent advances in the conversion of furfural into bio-chemicals through chemo- and bio-catalysis, RSC Adv. 11 (2021) 27042–27058, https://doi.org/10.1039/d1ra04633k.
[13] D.S.S. Jorqueira, L.F. de Lima, S.F. Moya, L. Vilcocq, D. Richard, M.A. Fraga, R. S. Suppino, Critical review of furfural and furfuryl alcohol production: past, present, and future on heterogeneous catalysis, Appl. Catal. A Gen. 665 (2023), https://doi.org/10.1016/j.apcata.2023.119360.
[14] A. Jaswal, P.P. Singh, T. Mondal, Furfural-a versatile, biomass-derived platform chemical for the production of renewable chemicals, Green Chem. 24 (2022) 510–551, https://doi.org/10.1039/d1gc03278j.
[15] C. Xu, E. Paone, D. Rodríguez-Padrón, R. Luque, F. Mauriello, Recent catalytic routes for the preparation and the upgrading of biomass derived furfural and 5-hydroxymethylfurfural, Chem. Soc. Rev. 49 (2020) 4273–4306, https://doi.org/10.1039/d0cs00041h.
[16] P. Khemthong, C. Yimsukanan, T. Narkkun, A. Srifa, T. Witoon, S. Pongchaiphol, S. Kiatphuengporn, K. Faungnawakij, Advances in catalytic production of value-added biochemicals and biofuels via furfural platform derived lignocellulosic biomass, Biomass Bioenergy 148 (2021) 106033, https://doi.org/10.1016/j.biombioe.2021.106033.
[17] M. Sankar, N. Dimitratos, P.J. Miedziak, P.P. Wells, C.J. Kiely, G.J. Hutchings, Designing bimetallic catalysts for a green and sustainable future, Chem. Soc. Rev. 41 (2012) 8099–8139, https://doi.org/10.1039/c2cs35296f.
[18] J. Park, U. Mushtaq, J.R. Sugiarto, D. Verma, J. Kim, Total chemocatalytic cascade conversion of lignocellulosic biomass into biochemicals, Appl. Catal. B Environ. 310 (2022) 121280, https://doi.org/10.1016/j.apcatb.2022.121280.
[19] K. Lee, Y. Jing, Y. Wang, N. Yan, A unified view on catalytic conversion of biomass and waste plastics, Nat. Rev. Chem. 6 (2022) 635–652, https://doi.org/10.1038/s41570-022-00411-8.
[20] W. Deng, Y. Feng, J. Fu, H. Guo, Y. Guo, B. Han, Z. Jiang, L. Kong, C. Li, H. Liu, P.T. T. Nguyen, P. Ren, F. Wang, S. Wang, Y. Wang, Y. Wang, S.S. Wong, K. Yan, N. Yan, X. Yang, Y. Zhang, Z. Zhang, X. Zeng, H. Zhou, Catalytic conversion of lignocellulosic biomass into chemicals and fuels, Green Energy Environ. 8 (2023) 10–114, https://doi.org/10.1016/j.gee.2022.07.003.
[21] R. Šivec, M. Huš, B. Likozar, M. Grilc, Furfural hydrogenation over Cu, Ni, Pd, Pt, Re, Rh and Ru catalysts: Ab initio modelling of adsorption, desorption and reaction micro-kinetics, Chem. Eng. J. 436 (2022) 32–40, https://doi.org/10.1016/j.cej.2022.135070.
[22] Z. An, J. Li, Recent advances in the catalytic transfer hydrogenation of furfural to furfuryl alcohol over heterogeneous catalysts, Green Chem. 24 (2022) 1780–1808, https://doi.org/10.1039/d1gc04440k.
[23] Q. Fu, H. Jiang, Y. Wang, H. Wang, X. Zhao, Recent advances in metal-organic framework based heterogeneous catalysts for furfural hydrogenation reactions, Mater. Chem. Front. 7 (2022) 628–642, https://doi.org/10.1039/d2qm01181f.
[24] J. Zhang, D.N. Li, H.R. Yuan, S.R. Wang, Y. Chen, Advances on the catalytic hydrogenation of biomass-derived furfural and 5-hydroxymethylfurfural, Ranliao Huaxue Xuebao/Journal Fuel Chem. Technol. 49 (2021) 1752–1767, https://doi.org/10.1016/S1872-5813(21)60135-4.
[25] A. Richel, P. Maireles-Torres, C. Len, Recent advances in continuous reduction of furfural to added value chemicals, Curr. Opin. Green Sustain. Chem. 37 (2022) 100655, https://doi.org/10.1016/j.cogsc.2022.100655.
[26] R.M. Mironenko, O.B. Belskaya, V.A. Likholobov, Aqueous-phase hydrogenation of furfural in the presence of supported metal catalysts of different types. A review, Dokl. Phys. Chem. 509 (2023) 33–50, https://doi.org/10.1134/S0012501623600109.
[27] S. Liu, N. Govindarajan, K. Chan, Understanding activity trends in furfural hydrogenation on transition metal surfaces, ACS Catal. 12 (2022) 12902–12910, https://doi.org/10.1021/acscatal.2c03822.
[28] S.K. Singh, Heterogeneous bimetallic catalysts for upgrading biomass-derived furans, Asian J. Org. Chem. 7 (2018) 1901–1923, https://doi.org/10.1002/ajoc.201800307.
[29] Z. Yu, X. Lu, X. Wang, J. Xiong, X. Li, R. Zhang, N. Ji, Metal-catalyzed hydrogenation of biomass-derived furfural: particle size effects and regulation strategies, ChemSusChem 13 (2020) 5185–5198, https://doi.org/10.1002/cssc.202001467.
[30] C. Wang, Z. Liu, L. Wang, X. Dong, J. Zhang, G. Wang, S. Han, X. Meng, A. Zheng, F.S. Xiao, Importance of zeolite wettability for selective hydrogenation of furfural over Pd@zeolite catalysts, ACS Catal. 8 (2018) 474–481, https://doi.org/10.1021/acscatal.7b03443.
[31] S. Campisi, C.E. Chan-Thaw, L.E. Chinchilla, A. Chutia, G.A. Botton, K.M. H. Mohammed, N. Dimitratos, P.P. Wells, A. Villa, Dual-site-mediated hydrogenation catalysis on Pd/NiO: selective biomass transformation and maintenance of catalytic activity at low Pd loading, ACS Catal. 10 (2020) 5483–5492, https://doi.org/10.1021/acscatal.0c00414.
[32] I.K.M. Yu, F. Deng, X. Chen, G. Cheng, Y. Liu, W. Zhang, J.A. Lercher, Impact of hydronium ions on the Pd-catalyzed furfural hydrogenation, Nat. Commun. 13 (2022) 4–12, https://doi.org/10.1038/s41467-022-34608-8.
[33] S.H. Pang, C.A. Schoenbaum, D.K. Schwartz, J.W. Medlin, Effects of thiol modifiers on the kinetics of furfural hydrogenation over Pd catalysts, ACS Catal. 4 (2014) 3123–3131, https://doi.org/10.1021/cs500598y.
[34] S.H. Pang, C.A. Schoenbaum, D.K. Schwartz, J.W. Medlin, Directing reaction pathways by catalyst active-site selection using self-assembled monolayers, Nat. Commun. 4 (2013) 1–6, https://doi.org/10.1038/ncomms3448.
[35] M.J. Islam, M. Granollers Mesa, A. Osatiashtiani, J.C. Manayil, M.A. Isaacs, M. J. Taylor, S. Tsatsos, G. Kyriakou, PdCu single atom alloys supported on alumina for the selective hydrogenation of furfural, Appl. Catal. B Environ. 299 (2021) 120652, https://doi.org/10.1016/j.apcatb.2021.120652.
[36] S.T. Thompson, H.H. Lamb, Palladium-rhenium catalysts for selective hydrogenation of furfural: evidence for an optimum surface composition, ACS Catal. 6 (2016) 7438–7447, https://doi.org/10.1021/acscatal.6b01398.
[37] Z.L. Wu, J. Wang, S. Wang, Y.X. Zhang, G.Y. Bai, L. Ricardez-Sandoval, G.C. Wang, B. Zhao, Controllable chemoselective hydrogenation of furfural by PdAg/C bimetallic catalysts under ambient operating conditions: an interesting Ag switch, Green Chem. 22 (2020) 1432–1442, https://doi.org/10.1039/c9gc03693h.
[38] L. Liu, H. Lou, M. Chen, Selective hydrogenation of furfural over Pt based and Pd based bimetallic catalysts supported on modified multiwalled carbon nanotubes (MWNT), Appl. Catal. A Gen. 550 (2018) 1–10, https://doi.org/10.1016/j.apcata.2017.10.003.
[39] K. Fulajtárova, T. Soták, M. Hronec, I. Vávra, E. Dobročka, M. Omastová, Aqueous phase hydrogenation of furfural to furfuryl alcohol over Pd-Cu catalysts, Appl. Catal. A Gen. 502 (2015) 78–85, https://doi.org/10.1016/j.apcata.2015.05.031.
[40] M. Hronec, K. Fulajtárová, I. Vávra, T. Soták, E. Dobročka, M. Mičušík, Carbon supported Pd-Cu catalysts for highly selective rearrangement of furfural to cyclopentanone, Appl. Catal. B Environ. 181 (2016) 210–219, https://doi.org/10.1016/j.apcatb.2015.07.046.
[41] S. Sitthisa, T. Pham, T. Prasomsri, T. Sooknoi, R.G. Mallinson, D.E. Resasco, Conversion of furfural and 2-methylpentanal on Pd/SiO2 and Pd-Cu/SiO2 catalysts, J. Catal. 280 (2011) 17–27, https://doi.org/10.1016/j.jcat.2011.02.006.
[42] R.M. Mironenko, O.B. Belskaya, A.V. Lavrenov, V.A. Likholobov, Palladium–ruthenium catalyst for selective hydrogenation of furfural to cyclopentanol, Kinet. Catal. 59 (2018) 339–346, https://doi.org/10.1134/S0023158418030151.
[43] G. Bagnato, M. Signoretto, C. Pizzolitto, F. Menegazzo, X. Xi, G.H. Ten Brink, B. J. Kooi, H.J. Heeres, A. Sanna, Hydrogenation of biobased aldehydes to monoalcohols using bimetallic catalysts, ACS Sustain. Chem. Eng. 8 (2020) 11994–12004, https://doi.org/10.1021/acssuschemeng.0c02623.
[44] L. Ruan, H. Zhang, M. Zhou, L. Zhu, A. Pei, J. Wang, K. Yang, C. Zhang, S. Xiao, B. H. Chen, A highly selective and efficient Pd/Ni/Ni(OH)2/C catalyst for furfural hydrogenation at low temperatures, Mol. Catal. 480 (2020) 110639, https://doi.org/10.1016/j.mcat.2019.110639.
[45] Y. Nakagawa, K. Takada, M. Tamura, K. Tomishige, Total hydrogenation of furfural and 5-hydroxymethylfurfural over supported Pd-Ir alloy catalyst, ACS Catal. 4 (2014) 2718–2726, https://doi.org/10.1021/cs500620b.
[46] M. Lesiak, M. Binczarski, S. Karski, W. Maniukiewicz, J. Rogowski, E. Szubiakiewicz, J. Berlowska, P. Dziugan, I. Witońska, Hydrogenation of furfural over Pd-Cu/Al2O3 catalysts. The role of interaction between palladium and copper on determining catalytic properties, J. Mol. Catal. A Chem. 395 (2014) 337–348, https://doi.org/10.1016/j.molcata.2014.08.041.
[47] X. Chang, A.F. Liu, B. Cai, J.Y. Luo, H. Pan, Y.B. Huang, Catalytic transfer hydrogenation of furfural to 2-methylfuran and 2-methyltetrahydrofuran over bimetallic copper–palladium catalysts, ChemSusChem 9 (2016) 3330–3337, https://doi.org/10.1002/cssc.201601122.
[48] N. Pino, S. Sitthisa, Q. Tan, T. Souza, D. López, D.E. Resasco, Structure, activity, and selectivity of bimetallic Pd-Fe/SiO2 and Pd-Fe/Γ-Al2O3 catalysts for the conversion of furfural, J. Catal. 350 (2017) 30–40, https://doi.org/10.1016/j.jcat.2017.03.016.
[49] S. Capelli, I. Barlocco, F.M. Scesa, X. Huang, D. Wang, F. Tessore, A. Villa, A. Di Michele, C. Pirola, Pd–Au bimetallic catalysts for the hydrogenation of muconic acid to bio-adipic acid, Catalysts 11 (2021) 1313, https://doi.org/10.3390/catal11111313.
[50] S. Campisi, S. Bellomi, L.E. Chinchilla, L. Prati, A. Villa, Base-free oxidative esterification of HMF over AuPd/nNiO-TiO 2. When alloying effects and metal-support interactions converge in producing effective and stable catalysts, ChemCatChem 14 (2022) 1–9, https://doi.org/10.1002/cctc.202200494.

[51] S. Campisi, S. Capelli, M. Ferri, A. Villa, E. Dann, A. Wade, P.P. Wells, N. Dimitratos, On the role of bismuth as modifier in AuPdBi catalysts: effects on liquid-phase oxidation and hydrogenation reactions, Catal. Commun. 158 (2021) 106340, https://doi.org/10.1016/j.catcom.2021.106340.

[52] S. Campisi, M. Stucchi, N. Dimitratos, A. Villa, A career in catalysis: Laura Prati, ACS Catal. 13 (2023) 1326–1348, https://doi.org/10.1021/acscatal.2c05237.

[53] A. Villa, D. Ferri, S. Campisi, C.E. Chan-Thaw, Y. Lu, O. Kröcher, L. Prati, Operando attenuated total reflectance FTIR spectroscopy: studies on the different selectivity observed in benzyl alcohol oxidation, ChemCatChem 7 (2015) 2534–2541, https://doi.org/10.1002/cctc.201500432.

[54] I. Barlocco, S. Capelli, X. Lu, S. Bellomi, X. Huang, D. Wang, L. Prati, N. Dimitratos, A. Roldan, A. Villa, Disclosing the role of gold on palladium – gold alloyed supported catalysts in formic acid decomposition, ChemCatChem 13 (2021) 4210–4222, https://doi.org/10.1002/cctc.202100886.

[55] L. Prati, A. Villa, A. Jouve, A. Beck, C. Evangelisti, A. Savara, Gold as a modifier of metal nanoparticles: effect on structure and catalysis, Faraday Discuss. 208 (2018) 395–407, https://doi.org/10.1039/c7fd00223h.

[56] M. Modelska, M.J. Binczarski, Z. Kaminski, S. Karski, B. Kolesinska, P. Mierczynski, C.J. Severino, A. Stanishevsky, I.A. Witonska, Bimetallic Pd-Au/SiO2 catalysts for reduction of furfural in water, Catalysts 10 (2020) 444, https://doi.org/10.3390/catal10040444.

[57] N.S. Date, V. La Parola, C.V. Rode, M.L. Testa, Ti-doped Pd-Au catalysts for one-pot hydrogenation and ring opening of furfural, Catalysts 8 (2018), https://doi.org/10.3390/catal8060252.

[58] B. Panella, A. Vargas, D. Ferri, A. Baiker, Chemical availability and reactivity of functional groups grafted to magnetic nanoparticles monitored in situ by ATR-IR spectroscopy, Chem. Mater. 21 (2009) 4316–4322, https://doi.org/10.1021/cm901665f.

[59] G. Kresse, J. Hafner, Ab initio molecular dynamics for liquid metals, Phys. Rev. B 47 (1993) 558–561, https://doi.org/10.1103/PhysRevB.47.558.

[60] G. Kresse, J. Hafner, Ab initio molecular-dynamics simulation of the liquid-metalamorphous- semiconductor transition in germanium, Phys. Rev. B 49 (1994) 14251–14269, https://doi.org/10.1103/PhysRevB.49.14251.

[61] G. Kresse, J. Furthmüller, Efficient iterative schemes for ab initio total-energy calculations using a plane-wave basis set, Phys. Rev. B - Condens. Matter Mater. Phys. 54 (1996) 11169–11186, https://doi.org/10.1103/PhysRevB.54.11169.

[62] J.P. Perdew, K. Burke, M. Ernzerhof, Generalized gradient approximation made simple, Phys. Rev. Lett. 77 (1996) 3865–3868, https://doi.org/10.1103/PhysRevLett.77.3865.

[63] P.E. Blöchl, Projector augmented-wave method, Phys. Rev. B 50 (1994) 17953–17979, https://doi.org/10.1103/PhysRevB.50.17953.

[64] D. Joubert, From ultrasoft pseudopotentials to the projector augmented-wave method, Phys. Rev. B - Condens. Matter Mater. Phys. 59 (1999) 1758–1775, https://doi.org/10.1103/PhysRevB.59.1758.

[65] S. Grimme, J. Antony, S. Ehrlich, H. Krieg, A consistent and accurate ab initio parametrization of density functional dispersion correction (DFT-D) for the 94 elements H-Pu, J. Chem. Phys. 132 (2010) 154104, https://doi.org/10.1063/1.3382344.

[66] A. Savara, C.E. Chan-Thaw, J.E. Sutton, D. Wang, L. Prati, A. Villa, Molecular origin of the selectivity differences between palladium and gold–palladium in benzyl alcohol oxidation: different oxygen adsorption properties, ChemCatChem 9 (2017) 253–257, https://doi.org/10.1002/cctc.201601295.

[67] S. Campisi, D. Motta, I. Barlocco, R. Stones, T.W. Chamberlain, A. Chutia, N. Dimitratos, A. Villa, Furfural adsorption and hydrogenation at the oxide-metal interface: evidence of the support influence on the selectivity of iridium-based catalysts, ChemCatChem (2022), https://doi.org/10.1002/cctc.202101700 n/a. e202101700.

[68] R.E. Palmer, N. Jian, A. Villa, N. Dimitratos, C.R.A. Catlow, A. Chutia, P.P. Wells, C.E. Chan-Thaw, S.M. Rogers, M. Perdjon, A. Thetford, Tandem site- and size-controlled Pd nanoparticles for the directed hydrogenation of furfural, ACS Catal. 7 (2017) 2266–2274, https://doi.org/10.1021/acscatal.6b03190.

[69] T. Fovanna, M. Nachtegaal, A.H. Clark, O. Kröcher, D. Ferri, Preparation, quantification, and reaction of Pd hydrides on Pd/Al2O3 in liquid environment, ACS Catal. 13 (2023) 3323–3332, https://doi.org/10.1021/acscatal.2c04791.

[70] S. Wang, V. Vorotnikov, D.G. Vlachos, Coverage-induced conformational effects on activity and selectivity: hydrogenation and decarbonylation of furfural on Pd(111), ACS Catal. 5 (2015) 104–112, https://doi.org/10.1021/cs5015145.

[71] M.J. Taylor, L. Jiang, J. Reichert, A.C. Papageorgiou, S.K. Beaumont, K. Wilson, A. F. Lee, J.V. Barth, G. Kyriakou, Catalytic hydrogenation and hydrodeoxygenation of furfural over Pt(111): a model system for the rational design and operation of practical biomass conversion catalysts, J. Phys. Chem. C 121 (2017) 8490–8497, https://doi.org/10.1021/acs.jpcc.7b01744.